

Interplay between crystallinity profiles and the performance of microcrystalline thin-film silicon solar cells studied by in-situ Raman spectroscopy

T. Fink, S. Muthmann, A. Mück, A. Gordijn, R. Carius, and M. Meier

Citation: [Journal of Applied Physics](#) **118**, 215304 (2015); doi: 10.1063/1.4936616

View online: <http://dx.doi.org/10.1063/1.4936616>

View Table of Contents: <http://scitation.aip.org/content/aip/journal/jap/118/21?ver=pdfcov>

Published by the [AIP Publishing](#)

Articles you may be interested in

[Light trapping in thin-film solar cells measured by Raman spectroscopy](#)

Appl. Phys. Lett. **105**, 111106 (2014); 10.1063/1.4895931

[Relationship between the cell thickness and the optimum period of textured back reflectors in thin-film microcrystalline silicon solar cells](#)

Appl. Phys. Lett. **102**, 053509 (2013); 10.1063/1.4790642

[Hydrogenated amorphous silicon oxide containing a microcrystalline silicon phase and usage as an intermediate reflector in thin-film silicon solar cells](#)

J. Appl. Phys. **109**, 113109 (2011); 10.1063/1.3592208

[In situ Auger electron spectroscopy studies of the growth of p -type microcrystalline silicon films on ZnO-coated glass substrates for microcrystalline silicon p-i-n solar cells](#)

Appl. Phys. Lett. **87**, 221908 (2005); 10.1063/1.2135883

[Optical and transport studies on thin microcrystalline silicon films prepared by very high frequency glow discharge for solar cell applications](#)

J. Appl. Phys. **81**, 7376 (1997); 10.1063/1.365354

A promotional banner for AIP Applied Physics Reviews. On the left is a small image of the journal cover for 'Applied Physics Reviews', which features a diagram of a device structure. The main part of the banner has a blue background with a molecular structure of spheres and sticks. The text 'NEW Special Topic Sections' is prominently displayed in white. Below this, on an orange background, it says 'NOW ONLINE' in yellow, followed by 'Lithium Niobate Properties and Applications: Reviews of Emerging Trends' in white. The AIP Applied Physics Reviews logo is in the bottom right corner.

NEW Special Topic Sections

NOW ONLINE
Lithium Niobate Properties and Applications:
Reviews of Emerging Trends

AIP Applied Physics Reviews

Interplay between crystallinity profiles and the performance of microcrystalline thin-film silicon solar cells studied by in-situ Raman spectroscopy

T. Fink, S. Muthmann, A. Mück, A. Gordijn, R. Carius, and M. Meier
IEK5-Photovoltaics, Forschungszentrum Jülich GmbH, 52428 Jülich, Germany

(Received 26 June 2015; accepted 14 November 2015; published online 7 December 2015)

The intrinsic microcrystalline absorber layer growth in thin-film silicon solar-cells is investigated by in-situ Raman spectroscopy during plasma enhanced chemical vapor deposition. In-situ Raman spectroscopy enables a detailed study of the correlation between the process settings, the evolution of the Raman crystallinity in growth direction, and the photovoltaic parameters η (solar cell conversion efficiency), J_{SC} (short circuit current density), FF (fill factor), and V_{OC} (open circuit voltage). Raman spectra were taken every 7 nm of the absorber layer growth depending on the process settings. The Raman crystallinity of growing microcrystalline silicon was determined with an absolute error of approximately $\pm 5\%$ for total absorber layer thicknesses > 50 nm. Due to this high accuracy, inherent drifts of the Raman crystallinity profiles are resolvable for almost the entire absorber layer deposition. For constant process settings and optimized solar cell device efficiency Raman crystallinity increases during the absorber layer growth. To compensate the inhomogeneous absorber layer growth process settings were adjusted. As a result, absorber layers with a constant Raman crystallinity profile — as observed in-situ — were deposited. Solar cells with those absorber layers show a strongly enhanced conversion efficiency by $\sim 0.5\%$ absolute. However, the highest FF , V_{OC} , and J_{SC} were detected for solar cells with different Raman crystallinity profiles. In particular, fill factors of 74.5% were observed for solar cells with decreasing Raman crystallinity during the later absorber layer growth. In contrast, intrinsic layers with favorable J_{SC} are obtained for constant and increasing Raman crystallinity profiles. Therefore, monitoring the evolution of the Raman crystallinity in-situ provides sufficient information for an optimization of the photovoltaic parameters with surpassing depth resolution. © 2015 AIP Publishing LLC.

[<http://dx.doi.org/10.1063/1.4936616>]

I. INTRODUCTION

Microcrystalline silicon (μc -Si:H) grown by plasma enhanced chemical vapor deposition (PECVD) is used as an absorber layer in thin-film solar cell stacks because of its high absorption coefficient for long wavelengths and due to the stability against light induced degradation.^{1–3} In the last two decades, a huge effort was made to enhance the material quality of μc -Si:H.^{4–8} Concerning the material quality of intrinsic absorber layers, crystalline volume fraction in the growth direction has a great impact on η , FF , V_{OC} and J_{SC} .¹ It is common practice to estimate the crystalline volume fraction by the Raman crystallinity.^{9,10}

The growth of μc -Si:H is influenced by a large number of external and internal process parameters (substrate morphology,¹¹ seeding effect of doping layers,¹² plasma excitation frequency,⁶ reactor geometry,¹³ etc.). Therefore, the reproducibility of Raman crystallinity profiles in the growth direction is challenging and optimized Raman crystallinities throughout the absorber layer are difficult to realize. To address this issue innovative diagnostic techniques and a more profound understanding of the interdependence between the PECVD process settings, the evolution of the Raman crystallinity, and the photovoltaic parameters is required.

At low Raman crystallinities below the percolation threshold the charge carrier mobility is restricted.¹⁴ For high

Raman crystallinities grain boundaries are poorly passivated and μc -Si:H exhibits high density of twin defects and voids.^{1,15,16} Although the conductivity is enhanced in this case, the density of recombination centers as well as the atmospheric gas incorporation is increased.^{1,17} The highest solar cell performances were detected for absorber layers with Raman crystallinities of about 60%–70%.^{1,12,15,18–20} The ideal evolution of the Raman crystallinity throughout the absorber layer is still a matter of debate. Therefore, this is one of the questions that will be addressed here.

In general, PECVD-inherent process drifts^{19,21} and the conical evolution of the crystallites^{1,9,22} for low Raman crystallinities impede a homogeneous absorber layer growth in the narrow deposition window close to 60%–70%.²¹ To achieve these Raman crystallinities throughout the entire absorber layer process settings have to be adapted during the deposition of μc -Si:H. Since this requires an adequate monitoring of the Raman crystallinity, various in-situ and ex-situ measurement techniques have been applied to characterize the μc -Si:H absorber layer deposition.^{8–10,12,13,19,21–28}

To monitor the layer growth with adequate accuracy, diagnostic methods with high depth and temporal resolution are required. For example, in-situ ellipsometry features high surface sensitivity.^{8,22} However, incident angles of 70° – 80° complicate the integration of the ellipsometry setup into the

parallel plate reactor and data analysis becomes difficult for varying substrate morphology.²⁹ The plasma emission of the PECVD process is recorded with excellent temporal resolution by optical emission spectroscopy (OES),^{13,25} but material properties of the growing layer are not probed. High depth resolution of the Raman crystallinity in the growth direction was achieved by KOH wet-etching or reactive ion etching.^{12,21,24} Scanning the etched craters by microscopic Raman spectroscopy, the Raman crystallinity is estimated in the growth direction of the $\mu\text{c-Si:H}$ film ex-situ.²⁴

In the present paper, we investigate the microcrystalline silicon growth by the technique of in-situ Raman spectroscopy.³⁰ This method enables the monitoring of the Raman crystallinity during the deposition of the absorber layer. It is possible to adjust the Raman excitation laser under perpendicular incidence to the probed surface, because an optimized electric shielding of the optical feed through was achieved.³¹ Moreover, data analysis is independent of the morphology of the growing film. The depth resolution of in-situ Raman spectroscopy is sufficient to investigate the initial deposition phase of $\mu\text{c-Si:H}$ absorber layers as well as to study the impact of the initial Raman crystallinity on the evolution of the later layer growth in detail. Muthmann *et al.* reported on the capabilities of that technique to study the Raman crystallinity during the initial growth phase and to observe the effect of an adjusted silane to hydrogen ratio.³² Here, we monitor the evolution of the Raman crystallinity throughout the entire intrinsic layer. The inhomogeneous absorber layer growth is successively compensated by an iterative readjustment of the process settings and the impact on the solar cell parameters is discussed.

II. EXPERIMENTAL

For the preparation of p-i-n single junction silicon solar cells in superstrate configuration with a $\mu\text{c-Si:H}$ intrinsic absorber layer a multi chamber system for the deposition on $10 \times 10 \text{ cm}^2$ corning glass was used. The approximately 30 nm thick microcrystalline boron doped p-type layers were grown on aluminum doped wet-etched zinc oxide substrates³³ (front contact). Although 30 nm thick p-layers are optically unfavorable, stable and reproducible starting conditions for the absorber layer deposition were provided. To complete the p-i-n single-junction solar cells (1300 ± 70) nm thick intrinsic absorber layers and amorphous phosphorous doped n-type layers were deposited. The back contact consists of thermally evaporated silver. An active solar cell area of $1 \times 1 \text{ cm}^2$ is defined by shadow masks for each single solar cell. The I-V-parameters were measured under AM 1.5 illuminations in a class A solar simulator. Each data point of the photovoltaic parameters was calculated by the average of the three best $1 \times 1 \text{ cm}^2$ solar cells. For this calculation absolute measurement errors of the photovoltaic parameters are $\Delta\eta = \pm 0.2\%$, $\Delta J_{\text{SC}} = \pm 0.5 \text{ mA/cm}^2$, $\Delta FF = \pm 0.5\%$, and $\Delta V_{\text{OC}} = \pm 5 \text{ mV}$. Solar cell conversion efficiency η and short circuit current density J_{SC} shown in this study are smaller than for recently reported record devices.^{34–36} Low J_{SC} most likely results from parasitic absorption in the comparably

thick p-layer and from plasmonic losses at the silver back contact.^{37,38}

For the plasma deposition of the intrinsic absorber layer an excitation frequency of 13.56 MHz in parallel plate electrode geometry with a power density of $\sim 0.4 \text{ W/cm}^2$ was applied. For the plasma etching experiments in Section III B, power density of $\sim 0.8 \text{ W/cm}^2$ differs from the other experiments of the manuscript. The substrate heater temperature was set to 200°C . The deposition pressure was kept constant at 10 Torr and the deposition gases were silane and hydrogen. From the gas flows of silane (Φ_{SiH_4}) and hydrogen (Φ_{H_2}) the silane concentration SC is defined as

$$SC = \frac{\Phi_{\text{SiH}_4}}{\Phi_{\text{SiH}_4} + \Phi_{\text{H}_2}}. \quad (1)$$

Silane concentration SC was changed significantly for the two-step process control. Nevertheless, the constant gas flow of hydrogen Φ_{H_2} (360 sccm) is roughly 2 orders of magnitude higher than the varied silane gas flow Φ_{SiH_4} (~ 3 sccm). Accordingly, the total gas flow rate was approximately constant during the absorber layer deposition. For the plasma etching experiments in Section III B, silane concentration was constant $SC = 1.4\%$.

To measure the Raman crystallinity in-situ, an optical feed through was integrated into the PECVD electrode.^{30,31} The Raman crystallinity was measured during the growth of the i-layer with a solid state Nd:YAG 532 nm laser. The information depth, which is probed by the laser, can be defined as the depth from which more than $2/e$ of the scattered Raman light originates. In our case, the information depth for a-Si:H and $\mu\text{c-Si:H}$ can be estimated to 56 nm and 125 nm for 532 nm excitation wavelength,³⁹ respectively. This implies that the Raman scattered light of the microcrystalline p-layer contributes to the Raman signal during the initial growth phase of the i-layer. However, for thin p-layer thicknesses of about 30 nm, the contribution is small. To reduce the heat input on the growing sample, the laser beam was chopped to 200 μs pulses (laser light exposure time) and the focus spot on the sample was broadened by a cylindrical lens. A temporal resolution of 25 s allows acquiring Raman spectra every ~ 7 nm of silicon film thickness when growth rates between 0.25 nm/s and 0.30 nm/s are assumed. For the analysis of the Raman spectra the reference spectrum of a pure amorphous sample was fitted to the data to determine the amorphous intensity contribution I_a of the Raman scattered light in the microcrystalline material.¹⁰ Accordingly, the Raman crystallinity is calculated as

$$I_{\text{C}}^{\text{RS}} = \frac{I_{\text{c}}}{I_{\text{c}} + I_{\text{a}}}, \quad (2)$$

in which I_{c} stands for the intensity contribution of the light scattered in the crystalline parts of the $\mu\text{c-Si:H}$ layer. To analyze the recorded spectra, different background signals were considered: On the one hand, the Raman scattered light of the optical components in the experimental setup, which stays constant during the deposition, was subtracted. On the other hand, the Raman scattered light of the corning glass

carrier material and the ZnO:Al front contact layer contributes to the i-layer signal during the initial growth phase. For the subtraction of this contribution the Raman intensity of the glass-ZnO:Al substrate was recorded prior to the p-layer deposition. From the data analysis of the Raman spectra, an absolute error of I_C^{RS} is estimated by $\Delta I_C^{RS} \leq \pm 5\%$ for silicon layer thicknesses $d > 50$ nm.

To compensate the inhomogeneous absorber layer growth, SC was readjusted in two steps (Fig. 1).

In region **A** the initial growth phase was investigated (Section III B). Here, a reduced initial silane concentration SC_i was applied to compensate the initially low I_C^{RS} . Therefore, SC_i was varied for an initial deposition time $t \leq 180$ s. For $t > 180$ s silane concentration SC was slightly increased and kept constant at 1.04% during the investigation of the initial growth phase (Fig. 1): It is well known that an increase of I_C^{RS} for the initial growth phase induces an overall increase of I_C^{RS} for the later layer growth.¹² Increasing SC avoids strongly deviating crystallinity from advantageous I_C^{RS} of $\sim 60\%$ – 70% ^{1,12,15,18–20} (Fig. 1). In a last step (Section III C), long-term drifts of I_C^{RS} , which occur for the later layer growth in region **B** (Fig. 1), were compensated by continuously changing SC with slope

$$\Delta SC = \frac{SC_B}{t_{\text{deposition}} - 180 \text{ s}}, \quad (3)$$

where SC_B stands for the total increase of SC in region **B** and $t_{\text{deposition}}$ denotes the total time of the i-layer deposition (ΔSC in units of %/h; h: hour).

III. RESULTS AND DISCUSSION

A. Crystallinity profiles for constant process settings

First, I_C^{RS} profiles for different constant silane concentrations during the i-layer deposition were recorded to study the influence of the process settings (SC) on the Raman crystallinity of the $\mu\text{c-Si:H}$ i-layer in the growth direction. Using this information it is possible to adapt the external process parameters to achieve a more homogeneous layer growth.

The crystallinity profiles during the deposition of the intrinsic $\mu\text{c-Si:H}$ layer are shown in Fig. 2, where the Raman

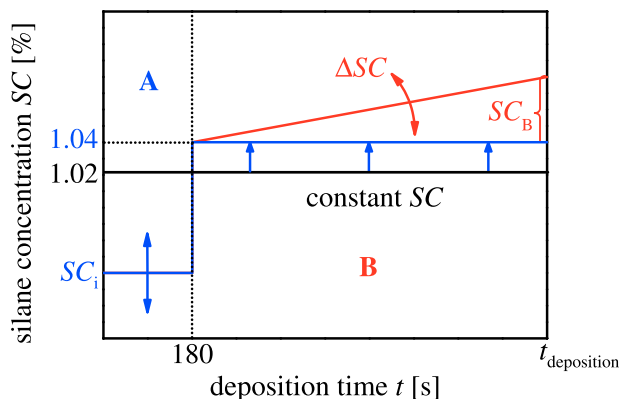


FIG. 1. Schematic of the silane concentration (SC) adjustment during absorber layer deposition: To study the influence on the initial growth phase (**A**), SC_i was varied ($t \leq 180$ s). To compensate the long-term drifts of the Raman crystallinity during the later layer growth, the silane concentration was changed with a slope of ΔSC (**B**).

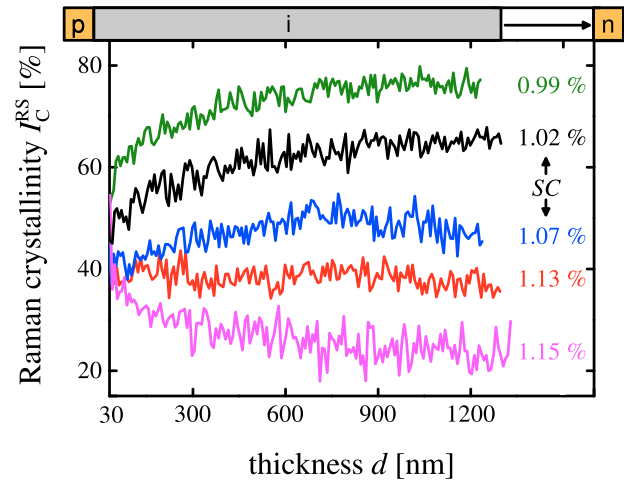


FIG. 2. Raman crystallinities I_C^{RS} of intrinsic microcrystalline silicon layers in dependence of the i-layer thickness for $d > 30$ nm, deposited at constant silane concentrations SC and measured by in-situ Raman spectroscopy.

crystallinity is plotted as a function of intrinsic layer thickness d . All crystallinity profiles start at a Raman crystallinity which is close to that of the p-layer ($\sim 58\%$). The upper two crystallinity profiles for $SC = 0.99\%$ and $SC = 1.02\%$ show strongly increasing I_C^{RS} at the beginning and a moderate increase of I_C^{RS} during the later layer growth. The lower two crystallinity profiles for $SC = 1.13\%$ and $SC = 1.15\%$ in Fig. 2 show decreasing I_C^{RS} during the deposition which is less pronounced for $SC = 1.13\%$. The crystallinity profile in the middle ($SC = 1.07\%$) features a reversing curve shape: At the beginning I_C^{RS} increases up to a thickness of ~ 700 – 800 nm and thereafter I_C^{RS} decreases again by $\sim 5\%$ absolute, which is in the range of the measurement error. Nevertheless, this effect was validated by the deposition of thick layers with $d > 2 \mu\text{m}$ and additionally by KOH crater etching experiments.⁴⁰

To explain the similar starting crystallinity of the Raman profiles close to that of the p-layer ($I_C^{RS} \approx 58\%$) two possible reasons have to be considered: One is the seeding effect of the p-layer which leads to a continuation of the crystalline growth, if deposition conditions are favorable. Additionally, the Raman scattered light partly originates from the p-layer during the initial growth phase due to the information depth of the 532 nm excitation laser.

For silane concentrations $SC = 0.99\%$ and $SC = 1.02\%$ low initial I_C^{RS} is observed compared to the later layer growth (Fig. 2). Low initial I_C^{RS} results from transient depletion of the process gases which typically occurs in PECVD processes.^{13,23,41} For the subsequent layer growth crystallites evolve conically and I_C^{RS} increases.^{1,9}

Decreasing I_C^{RS} under comparably high SC conditions was also observed previously by TEM measurements:⁹ In these experiments thin-film silicon was grown on crystalline silicon substrates for process conditions which promote low I_C^{RS} . In this case, the microstructure of $\mu\text{c-Si:H}$ material differs from conically growing crystallites and resembles randomly shaped crystallites surrounded by a-Si:H.^{9,42}

The reversing curve shape for $SC = 1.07\%$ might be explained by different process drifts which compensate each other over time.¹⁹

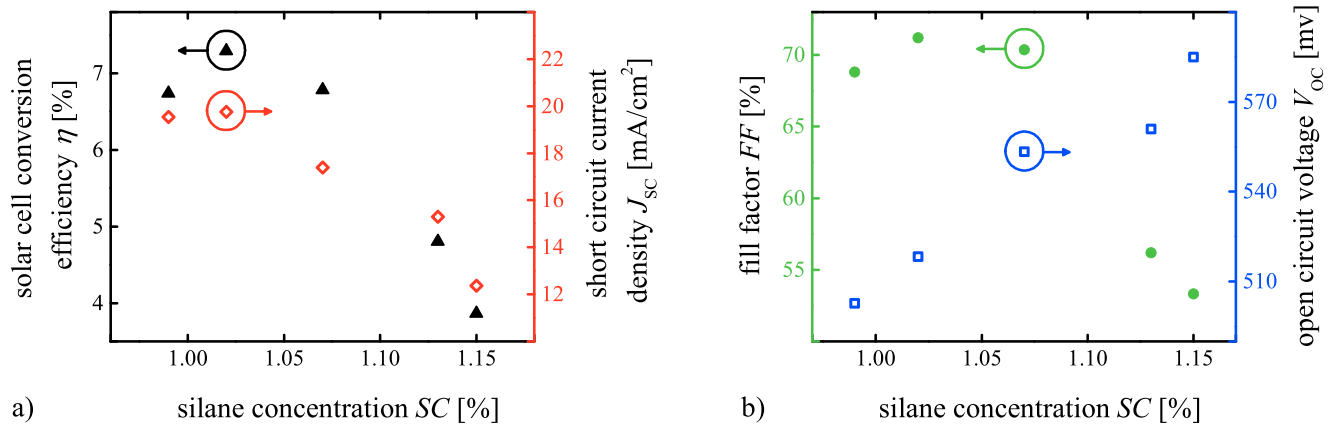


FIG. 3. (a) Solar cell conversion efficiency η resp. short circuit current density J_{sc} and (b) fill factor FF resp. open circuit voltage V_{oc} in dependence of the silane concentration SC . Maximum absolute measurement errors of the determined photovoltaic parameters are $\Delta\eta = \pm 0.2\%$, $\Delta J_{sc} = \pm 0.5 \text{ mA/cm}^2$, $\Delta FF = \pm 0.5\%$ and $\Delta V_{oc} = \pm 5 \text{ mV}$.

The Raman profiles shown in Fig. 2 provide direct information about the evolution of Raman crystallinity in $\mu\text{c-Si:H}$ absorber layers. To correlate the I_C^{RS} profiles with the device performance, conversion efficiency η , short circuit current density J_{sc} , fill factor FF , and open circuit voltage V_{oc} were measured (Fig. 3). As expected,¹ V_{oc} is increasing with increasing SC . The fill factor exhibits a maximum of 71.2% for $SC = 1.02\%$. At the same SC the solar cell conversion efficiency η has its maximum at $\eta = 7.29\%$ and drops for higher SC . In the considered SC range the highest J_{sc} and η are observed for $SC \approx 1.02\%$.

For constant process settings, the maximum of η (Fig. 3(a)) is achieved for $SC = 1.02\%$. The crystallinity profile for $SC = 1.02\%$ shows an average I_C^{RS} close to 60% and increases by about 15%–20% absolutely over the thickness of the intrinsic layer (Fig. 2). High depth resolution of in-situ Raman spectroscopy enables estimation of the adjustment of SC which is required to realize homogeneous layer growth.

B. Effects of modified Raman-crystallinity during the initial growth phase

As described above, low SC was applied to increase I_C^{RS} of the i-layer close to the p-type layer. Beforehand, the growth rate of the initial layer was estimated. For this reason, a sequence of thin layers was deposited and the layer

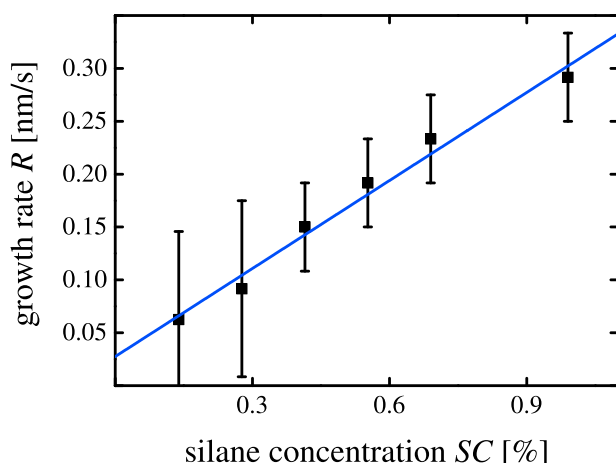


FIG. 4. Growth rate R as a function of silane concentration SC .

thickness was determined by a profilometer (Fig. 4). The growth rate increases approximately linearly with SC according to literature.^{43–45} After a deposition time $t_i = 180 \text{ s}$ of the $\mu\text{c-Si:H}$ i-layer, the layer thickness for $SC = 1.02\%$ is approximately 50 nm. Up to this thickness, the highest rate of change is observed in terms of the crystallinity evolution (Fig. 2).

An optimum of the device performance is expected when SC_i is decreased because for initially high SC_i of 1.02% unfavorable Raman crystallinity $I_C^{RS} < 60\%$ was obtained at the beginning of the i-layer growth (Fig. 2). To find out the deposition conditions for optimum device performance, SC_i was reduced and varied.

The photovoltaic parameters η , J_{sc} , FF , and V_{oc} of solar cells deposited with and without changing the initial silane concentration SC_i are shown in Fig. 5. A maximum of the solar cell conversion efficiency η is observed for $SC_i = 0.83\%$ (Fig. 5(a)). Compared to the results under constant deposition conditions ($SC_i = 1.02\%$), η was increased by $\sim 0.4\%$ absolute. Short circuit current density J_{sc} is improved by approximately 1 mA/cm^2 for reduced SC_i . Fill factor FF as well as V_{oc} are shown in Fig. 5(b): In comparison to the reference ($SC_i = 1.02\%$), FF is slightly increased in the range between $SC_i = 0.61\%$ and $SC_i = 0.83\%$. In contrast, V_{oc} features no local maximum and decreases by almost 20 mV for decreasing SC_i .

Obviously, the local maximum of η results from opposing trends of increasing J_{sc} and decreasing V_{oc} for reduced initial SC_i .

Since the initial growth phase of the i-layer is changed, we investigated J_{sc} wavelength dependent by measuring the external quantum efficiency EQE . In Fig. 6, EQE is shown for constant process settings ($SC = 1.02\%$) and for decreased initial SC_i ($t \leq 180 \text{ s}$, $SC(t > 180 \text{ s}) = 1.04\%$): In the long wavelength range for $\lambda > 700 \text{ nm}$, no significant modification of EQE is observed. For wavelengths $\lambda < 550 \text{ nm}$ and $SC = 1.02\%$ EQE is not varied significantly with and without reverse bias voltage V_{Bias} (Fig. 6). For slightly decreased initial SC_i from $SC_i = 1.02\%$ to $SC_i = 0.91\%$ EQE is enhanced and total J_{sc} is increased from 19.6 mA/cm^2 to 20.3 mA/cm^2 (Fig. 5(a)). The significance of this result is substantiated by an absolute error of $\Delta EQE = \pm 2\%$ resp. $\Delta J_{sc} = \pm 0.5 \text{ mA/cm}^2$. A further decrease of SC_i ($SC_i < 0.91\%$) results in minor changes of EQE and J_{sc} only (Figs. 5(a) and 6).

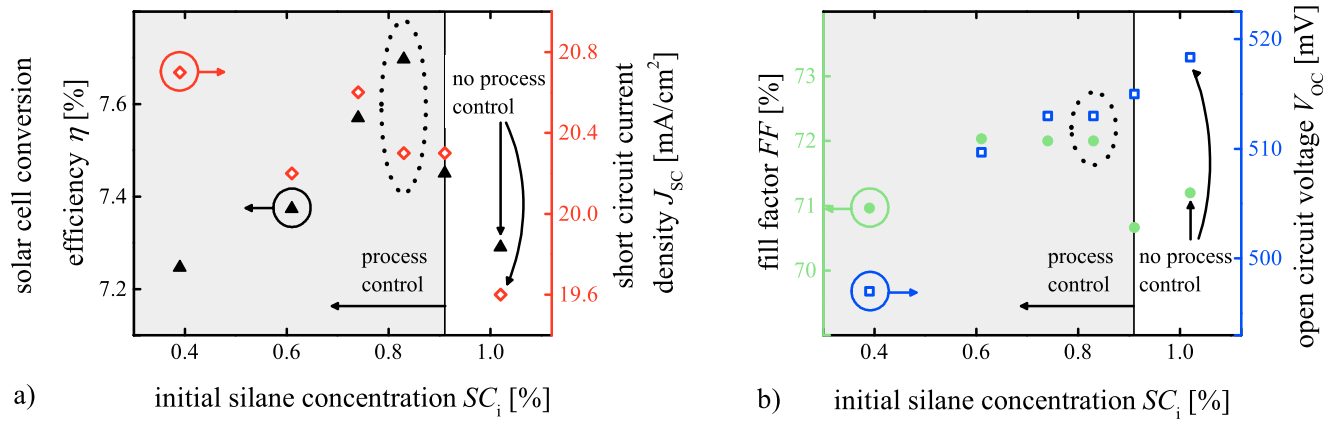


FIG. 5. (a) Solar cell conversion efficiency η resp. short circuit current density J_{sc} and (b) fill factor FF resp. open circuit voltage V_{oc} as a function of initial silane concentration SC_i ($SC(t > 180 \text{ s}) = 1.04\%$). The data points at $SC_i = 1.02\%$ (constant SC) represents the reference. Maximum absolute measurement errors of the determined photovoltaic parameters are $\Delta\eta = \pm 0.2\%$, $\Delta J_{sc} = \pm 0.5 \text{ mA/cm}^2$, $\Delta FF = \pm 0.5\%$ and $\Delta V_{oc} = \pm 5 \text{ mV}$.

After the adjustment of SC_i Raman crystallinity I_C^{RS} was monitored to study the phase mixture of the initial growth phase for the observed optimum of the device efficiency. In-situ Raman spectra are shown in Fig. 7 for $SC_i = 1.02\%$ (constant process settings with low initial I_C^{RS}) and $SC = 0.83\%$ (SC_i with local maximum of η). The spectra were recorded at $t_i = 180 \text{ s}$, for which the deposited layers exhibit thicknesses of $\sim 45\text{--}55 \text{ nm}$. For $SC_i = 1.02\%$ the Raman crystallinity is estimated to $I_C^{RS} = 50\%$. For $SC_i = 0.83\%$ Raman crystallinity $I_C^{RS} = 62\%$ is observed. These measurements show that even slight changes of the initial I_C^{RS} can be monitored by in-situ Raman spectroscopy and a well-defined adaption of the Raman crystallinity is enabled by changing the external process settings.

Due to the higher I_C^{RS} during the initial growth phase ($SC = 0.83\%$), increased defect density of the absorber layer material could be the reason for decreasing V_{oc} in Fig. 5(b).¹⁶ However, slightly increased FF for solar cells deposited with $SC = 0.83\%$ indicates moderately decreasing recombination loss in the absorber layer (Fig. 5). Therefore, we suppose that decreasing V_{oc} is not caused by higher defect density of the absorber layer. In addition, moderately

reduced charge carrier recombination probability cannot be responsible for the strongly enhanced EQE only (Fig. 6).

Alternatively, the hydrogen rich plasma at the beginning of the absorber layer growth could be an explanation for decreasing V_{oc} and increasing EQE in the short wavelength range. Several effects are conceivable: The growth rate at the very beginning of the intrinsic layer deposition is not known exactly (Fig. 4). Consequently, a short etching period during the very beginning of the absorber layer growth cannot be excluded. In addition the Raman crystallinity of the subsurface layers (p-layer) can be increased.^{46–48} Since the absorption coefficient of $\mu\text{c-Si:H}$ depends on I_C^{RS} ,^{25,49} the transparency of the p-layer might be enhanced. In both cases, an increase of the charge carrier generation could cause the improved EQE for initially low SC_i . Furthermore, the passivation of the doping atoms by hydrogen radicals^{50,51} could lead to a reduced built-in voltage of the solar cell.

To study the possible impact of a hydrogen plasma on the p-layer properties, a separate test experiment was performed: 30 nm p-type layers were treated with pure hydrogen plasma for a varying treatment time $t_{H\text{plasma}}$ of 50 s, 100 s, and 200 s. Open circuit voltage V_{oc} , FF and EQE of p-i-n

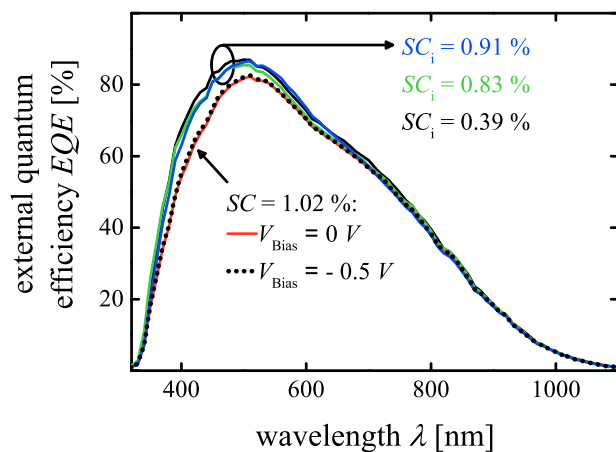


FIG. 6. External quantum efficiency EQE for solar cells deposited with decreasing initial silane concentration SC_i ($t \leq 180 \text{ s}$, $SC(t > 180 \text{ s}) = 1.04\%$) and for constant $SC = 1.02\%$ in dependence of the wavelength λ . For $SC_i = 1.02\%$ EQE measurements with and without reverse bias voltage V_{Bias} are depicted.

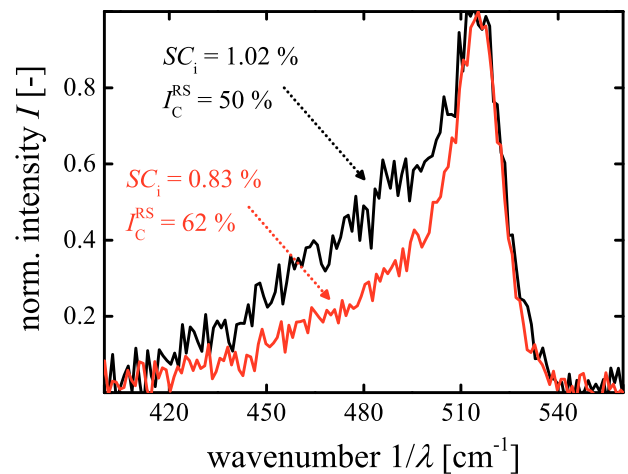


FIG. 7. Process control to increase the Raman crystallinity I_C^{RS} for the initial growth phase of the absorber layer deposition. The single in-situ Raman spectrum for 50 nm thickness of the second highest crystallinity profile in Fig. 2 is shown ($SC = 1.02\%$). To increase $I_C^{RS} = 50\%$ the initial silane concentration was decreased to $SC_i = 0.83\%$ and $I_C^{RS} = 62\%$ was achieved.

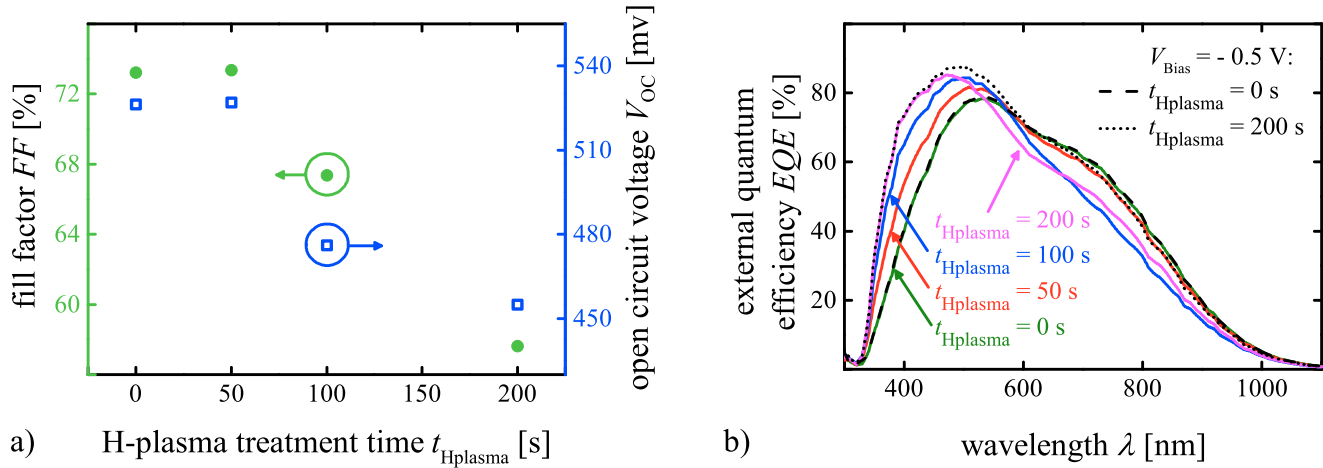


FIG. 8. (a) Open circuit voltage V_{OC} and fill factor FF as a function of the hydrogen plasma treatment time $t_{Hplasma}$. Maximum absolute measurement errors of the determined photovoltaic parameters are $\Delta FF = \pm 0.5\%$ and $\Delta V_{OC} = \pm 5$ mV. For the deposition of the i-layers a constant $SC = 1.4\%$ was used. (b) External quantum efficiency EQE for a series of solar cells, whose p-layers were treated by hydrogen plasma, as a function of the wavelength λ .

solar cells deposited on the pretreated p-layers are shown in Fig. 8 (i-layer deposition: $SC = 1.4\%$). For a short treatment time of 50 s, FF and V_{OC} are not affected. However, for longer treatment times of the p-type layer with hydrogen, FF and V_{OC} are significantly reduced. External quantum efficiency EQE decreases in the long wavelength range with increasing $t_{Hplasma}$ (Fig. 8(b)). In contrast, EQE is strongly enhanced in the short wavelength range for increasing $t_{Hplasma}$.^{52,53} This effect already appears for $t_{Hplasma} = 50$ s, although EQE of the longer wavelength range is not significantly decreased.

The loss of EQE for long wavelengths can be explained by the lowered built-in voltage of the solar cells because EQE increases again with reverse bias-voltage (Fig. 8(b) for $t_{Hplasma} = 200$ s). EQE with reverse bias voltage is not increased in the short wavelength range (Fig. 8(b): $t_{Hplasma} = 0$ s and $t_{Hplasma} = 200$ s). Consequently, improved EQE for extended $t_{Hplasma}$ is most probably caused by the optical modification of the pretreated p-layers.

In summary, EQE is increased in the short wavelength range for reduced SC_i from 1.02% to 0.91% and saturates for $SC_i < 0.91\%$ (Fig. 6). EQE of the solar cell deposited with

constant $SC = 1.02\%$ shows no improvement by applying reverse bias voltage V_{Bias} . This indicates that the increase of EQE for decreasing SC_i is related to changes of the optical performance of the solar cell (Fig. 6). Optical modifications were observed for solar cells with p-layers that were treated by hydrogen plasma (Fig. 8(b)). Although the outcome of this experiment cannot explain the saturation effect for decreased SC_i , it provides a qualitative explanation for the increase of EQE in the blue wavelength range (Fig. 6) by modifications of the p-layer transparency.

C. Effects of modified Raman-crystallinity during the later layer growth

The initial growth phase of the intrinsic μc -Si:H layer was optimized resulting in a I_C^{RS} of $\sim 60\%$ (Fig. 7). To optimize the growth in region B (Fig. 2), SC was changed continuously during the deposition to compensate increasing I_C^{RS} . In Fig. 9 crystallinity profiles are shown for varying ΔSC . The adaption of the initial SC results in a constant I_C^{RS} at $\sim 60\%$ for the first 400 nm of the i-layer deposition (Fig. 9). For small or negative ΔSC the Raman crystallinity increases during the deposition (I: $\Delta SC = -0.11\%/h$). For large positive ΔSC , I_C^{RS} decreases significantly (III: $\Delta SC = 0.11\%/h$). An almost constant crystallinity profile is found for $\Delta SC = 0.04\%/h$ (II). Only at the end of the 1300 nm thick i-layer the Raman crystallinity decreases slightly below 60%.

To correlate I_C^{RS} with device performance η , J_{SC} , FF and V_{OC} are studied (Fig. 10). Maximum solar cell conversion efficiencies of $\eta \approx (7.7 \pm 0.2)\%$ are observed between $\Delta SC = -0.06\%/h$ and $\Delta SC = 0.07\%/h$ (Fig. 10(a)). Within this range of ΔSC Raman crystallinities vary between approximately $I_C^{RS} = 60\%$ and $I_C^{RS} = 70\%$ during the later absorber layer growth (Fig. 9). Since this includes constant ΔSC readjustment of the process settings in region B seems to be dispensable. To demonstrate the importance of the controlled deposition photovoltaic parameters J_{SC} , FF , and V_{OC} are discussed in detail.

Highest $J_{SC} \approx 20.8 \text{ mA/cm}^2$ were achieved for $\Delta SC = -0.06\%/h$ and $\Delta SC = 0\%/h$, respectively (Fig. 10(a)). Slightly decreasing J_{SC} is detected for $\Delta SC < -0.06\%/h$,

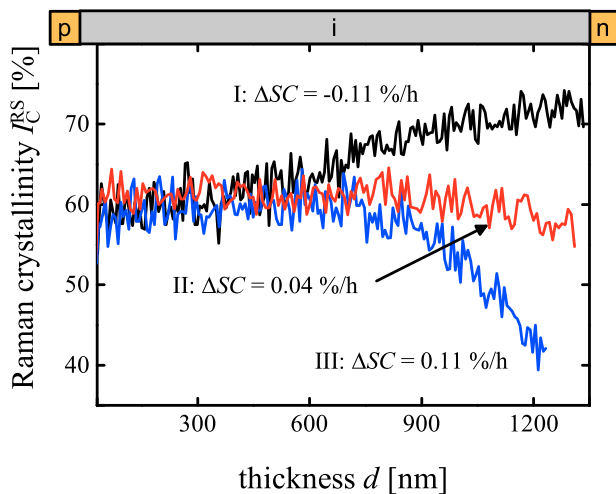


FIG. 9. Raman crystallinity I_C^{RS} as a function of thickness d for three different slopes of the silane concentration ΔSC .

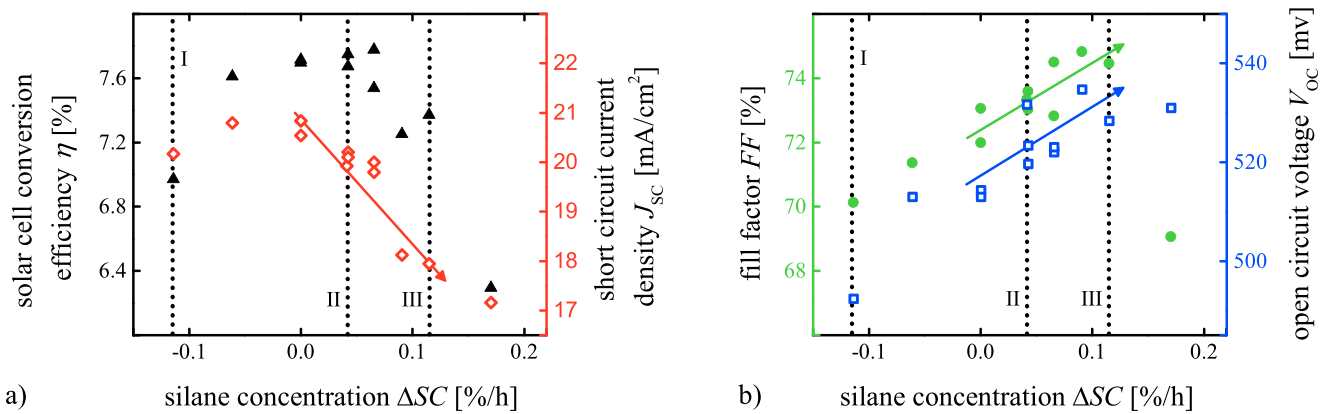


FIG. 10. Solar cell conversion efficiency η and short circuit current density J_{SC} in dependence of the silane concentration ΔSC . For three selected ΔSC , crystallinity profiles of the i-layer are shown in Fig. 9. (b) Fill factor FF and open circuit voltage V_{OC} as a function of ΔSC . Maximum absolute measurement errors of the determined photovoltaic parameters are $\Delta\eta = \pm 0.2\%$, $\Delta J_{SC} = \pm 0.5 \text{ mA/cm}^2$, $\Delta FF = \pm 0.5\%$ and $\Delta V_{OC} = \pm 5 \text{ mV}$.

whereas J_{SC} is reduced significantly for $\Delta SC > 0\%/h$. Strongly reduced J_{SC} between $\Delta SC = 0\%/h$ and $\Delta SC = 0.11\%/h$ is mainly caused by decreasing I_C^{RS} (Fig. 9) and decreased absorption coefficient of the intrinsic layer.⁵⁴ In contrast, decreasing J_{SC} for $\Delta SC < -0.06\%/h$ cannot be explained by the enhanced absorption coefficient of the intrinsic layer.⁵⁴

Fill factor FF is improved from $FF \approx 70\%$ to $FF \approx 75\%$ for increasing ΔSC from $-0.11\%/h$ to $0.11\%/h$ (Fig. 10(b)). For $\Delta SC = 0.17\%$ FF is significantly reduced to $FF \approx 69\%$. Open circuit voltage V_{OC} is enhanced over the entire studied range of ΔSC from about 490 mV to roughly 530 mV. Consequently, decreasing J_{SC} for $\Delta SC < -0.06\%/h$ (Fig. 10(a)) is most likely caused by the lowered FF .

As a result, maximum FF resp. V_{OC} and J_{SC} are found for different process settings and different Raman crystallinity profiles of the absorber layer. Between profile I ($\Delta SC = -0.11\%/h$) and II ($\Delta SC = 0.04\%/h$), evolution of the Raman crystallinity is favorable for J_{SC} . For Raman crystallinities between profile II ($\Delta SC = 0.04\%/h$) and III ($\Delta SC = 0.11\%/h$), FF resp. V_{OC} are improved. Compared to current record $\mu\text{-Si:H}$ single junction solar cells,^{18,36} fill factor and V_{OC} are quite similar ($0.04\%/h \leq \Delta SC \leq 0.11\%/h$), whereas the short circuit current density of these cells is superior to our device.

For constant Raman crystallinity profiles at approximately $I_C^{RS} = 60\%$, solar cell conversion efficiency is improved. However, since the solar cell parameters FF , V_{OC} and J_{SC} show maxima for different crystallinity profiles, ideal evolution of the Raman crystallinity remains unclear. Further improvement of the device performance might be achieved by a fine-tuning of the process settings. Monitoring the Raman crystallinity in-situ provides sufficient information to adjust the external process settings tailored to the requirements and enables the reproduction of high quality absorber layers.

IV. SUMMARY

In this paper, we investigated the effect of controlled absorber layer growth on the solar cell device performance. For this purpose, the Raman crystallinity was monitored during the absorber layer growth in-situ and growth drifts were compensated by readjusting the process settings.

First, crystallinity profiles deposited under constant process settings were studied in detail. Low Raman crystallinity at the initial growth phase and continuous drifts for the later layer deposition were detected.

To adapt the Raman crystallinity during the initial absorber layer growth, decreased initial silane concentration was applied. Due to the adjustment of the process settings the external quantum efficiency in the short wavelength range was enhanced and the solar cell conversion efficiency was improved by 0.41% absolute. For the compensation of the continuous increase of I_C^{RS} during the later layer growth, the silane concentration was gradually increased. Accordingly, a constant Raman crystallinity profile was achieved with $I_C^{RS} \approx 60\%$ throughout the entire absorber layer. Although solar cells with those absorber layers exhibit improved device efficiency, optimum photovoltaic parameters J_{SC} , FF and V_{OC} were obtained for different controlled Raman crystallinity profiles.

In conclusion, we demonstrated the controlled deposition of intrinsic microcrystalline absorber layers by monitoring the evolution of the Raman crystallinity in-situ, adjusting the process settings and observing the impact on the solar cell device parameters. Using this method, process drifts were compensated and beneficial crystallinity profiles were identified. Most likely, optimized crystallinity profiles as well as inherent process drifts vary dependent on the device configuration. Nevertheless, the presented iterative optimization procedure between the monitoring of the Raman crystallinity and the readjustment of the process settings is universally applicable.

¹O. Vetterl, F. Finger, R. Carius, P. Hapke, L. Houben, O. Kluth, A. Lambert, A. Mück, B. Rech, and H. Wagner, *Sol. Energy Mater. Sol. Cells* **62**, 97 (2000).

²J. Meier, S. Dubail, R. Fluckiger, D. Fischer, H. Keppner, and A. Shah, in *IEEE Proceedings of Intrinsic microcrystalline silicon ($\mu\text{-Si:H}$)-a promising new thin film solar cell material*, Waikoloa, HI, 1994, p. 409.

³J. Meier, S. Dubail, J. Cuperus, U. Kroll, R. Platz, P. Torres, J. A. Selvan, P. Pernet, N. Beck, and N. P. Vaucher, *J. Non-Cryst. Solids* **227**, 1250 (1998).

⁴G. Bugnon, G. Parascandolo, T. Söderström, P. Cuony, M. Despeisse, S. Hänni, J. Holovsky, F. Meillaud, and C. Ballif, *Adv. Funct. Mater.* **22**, 3665 (2012).

⁵M. Kondo, *Sol. Energy Mater. Sol. Cells* **78**, 543 (2003).

- ⁶F. Finger, P. Hapke, M. Luysberg, R. Carius, H. Wagner, and M. Scheib, *Appl. Phys. Lett.* **65**, 2588 (1994).
- ⁷B. Yan, G. Yue, Y. Yan, C.-S. Jiang, C. W. Teplin, J. Yang, and S. Guha, *MRS Online Proc. Libr.* **1066**, 61 (2008).
- ⁸R. W. Collins, A. S. Ferlauto, G. M. Ferreira, C. Chen, J. Koh, R. J. Koval, Y. Lee, J. M. Pearce, and C. R. Wronski, *Sol. Energy Mater. Sol. Cells* **78**, 143 (2003).
- ⁹L. Houben, M. Luysberg, P. Hapke, R. Carius, F. Finger, and H. Wagner, *Philos. Mag. A* **77**, 1447 (1998).
- ¹⁰C. Smit, R. A. C. M. M. van Swaaij, H. Donker, A. M. H. N. Petit, W. M. M. Kessels, and M. C. M. van de Sanden, *J. Appl. Phys.* **94**, 3582 (2003).
- ¹¹D. Y. Kim, R. Santbergen, K. Jäger, M. Sever, J. Krč, M. Topič, S. Hänni, C. Zhang, A. Heidt, M. Meier, R. A. C. M. M. van Swaaij, and M. Zeman, *ACS Appl. Mater. Interfaces* **6**, 22061 (2014).
- ¹²S. N. Agbo, S. Dobrovolskiy, G. Wegh, R. A. C. M. M. van Swaaij, F. D. Tichelaar, P. Sutta, and M. Zeman, *Prog. Photovoltaics* **22**, 346 (2014).
- ¹³A. A. Howling, B. Strahm, P. Colsters, L. Sansonnens, and C. Hollenstein, *Plasma Sources Sci. Technol.* **16**, 679 (2007).
- ¹⁴R. Carius, F. Finger, U. Backhausen, M. Luysberg, P. Hapke, L. Houben, M. Otte, and H. Overhof, *MRS Online Proc. Libr.* **467**, 283 (1997).
- ¹⁵B. Yan, G. Yue, J. Yang, S. Guha, D. L. Williamson, D. Han, and C.-S. Jiang, *Appl. Phys. Lett.* **85**, 1955 (2004).
- ¹⁶A. L. B. Neto, A. Lambertz, R. Carius, and F. Finger, *J. Non-Cryst. Solids* **299–302**, Part 1, 274 (2002).
- ¹⁷S. Michard, M. Meier, U. Zastrow, O. Astakhov, and F. Finger, *Can. J. Phys.* **92**, 774 (2014).
- ¹⁸S. Hänni, D. T. L. Alexander, L. Ding, G. Bugnon, M. Boccard, C. Battaglia, P. Cuony, J. Escarre, G. Parascandolo, S. Nicolay, M. Cantoni, M. Despeisse, F. Meillaud, and C. Ballif, *IEEE J. Photovoltaics* **3**, 11 (2013).
- ¹⁹M. N. van den Donker, T. Kilper, D. Grunsky, B. Rech, L. Houben, W. M. M. Kessels, and M. C. M. van de Sanden, *Thin Solid Films* **515**, 7455 (2007).
- ²⁰Y. Mai, S. Klein, R. Carius, J. Wolff, A. Lambertz, F. Finger, and X. Geng, *J. Appl. Phys.* **97**, 114913 (2005).
- ²¹V. Smirnov, C. Das, T. Melle, A. Lambertz, M. Hülsbeck, R. Carius, and F. Finger, *Mater. Sci. Eng. B* **159–160**, 44 (2009).
- ²²H. Fujiwara, M. Kondo, and A. Matsuda, *Phys. Rev. B* **63**, 115306 (2001).
- ²³T. Kilper, M. N. van den Donker, R. Carius, B. Rech, G. Bräuer, and T. Repmann, *Thin Solid Films* **516**, 4633 (2008).
- ²⁴F. Köhler, S. Schicho, B. Wolfrum, A. Gordijn, S. E. Pust, and R. Carius, *Thin Solid Films* **520**, 2605 (2012).
- ²⁵M. Meier, S. Muthmann, A. J. Flikweert, G. Dingemans, M. C. M. van de Sanden, and A. Gordijn, *Sol. Energy Mater. Sol. Cells* **95**, 3328 (2011).
- ²⁶G. Choong, E. Vallat-Sauvain, X. Multone, L. Fesquet, U. Kroll, and J. Meier, *J. Phys. D: Appl. Phys.* **46**, 235105 (2013).
- ²⁷H. Yue, A. Wu, X. Zhang, and T. Li, *J. Cryst. Growth* **322**, 1 (2011).
- ²⁸E. Vallat-Sauvain, U. Kroll, J. Meier, A. Shah, and J. Pohl, *J. Appl. Phys.* **87**, 3137 (2000).
- ²⁹H. Fujiwara, *Spectroscopic Ellipsometry* (John Wiley & Sons, Ltd., 2007), p. 369.
- ³⁰S. Muthmann, F. Köhler, M. Meier, M. Hülsbeck, R. Carius, and A. Gordijn, *Phys. Status Solidi RRL* **5**, 144 (2011).
- ³¹S. Muthmann, M. Meier, R. Schmitz, W. Appenzeller, A. Mück, and A. Gordijn, *Surf. Coat. Technol.* **205**, Supplement 2, S415 (2011).
- ³²S. Muthmann, F. Köhler, M. Meier, M. Hülsbeck, R. Carius, and A. Gordijn, *J. Non-Cryst. Solids* **358**, 1970 (2012).
- ³³M. Berginski, J. Hüpkes, M. Schulte, G. Schöpe, H. Stiebig, B. Rech, and M. Wuttig, *J. Appl. Phys.* **101**, 074903 (2007).
- ³⁴S. Hänni, G. Bugnon, G. Parascandolo, M. Boccard, J. Escarré, M. Despeisse, F. Meillaud, and C. Ballif, *Prog. Photovoltaics* **21**, 821 (2013).
- ³⁵H. Sai, T. Matsui, K. Matsubara, M. Kondo, and I. Yoshida, *IEEE J. Photovoltaics* **4**, 1349 (2014).
- ³⁶H. Sai, K. Maejima, T. Matsui, T. Koida, M. Kondo, S. Nakao, Y. Takeuchi, H. Katayama, and S. Yoshida, *Jpn. J. Appl. Phys., Part 1* **54**, 08KB05 (2015).
- ³⁷J. Springer, A. Poruba, L. Müllerova, M. Vanecek, O. Kluth, and B. Rech, *J. Appl. Phys.* **95**, 1427 (2004).
- ³⁸F.-J. Haug, T. Söderström, O. Cubero, V. Terrazzoni-Daudrix, and C. Ballif, *J. Appl. Phys.* **104**, 064509 (2008).
- ³⁹O. Vetterl, Ph.D. thesis, Universität Düsseldorf, 2001.
- ⁴⁰F. Urbain, V. Smirnov, J.-P. Becker, U. Rau, F. Finger, J. Ziegler, B. Kaiser, and W. Jaegermann, *J. Mater. Res.* **29**, 2605 (2014).
- ⁴¹M. N. van den Donker, B. Rech, W. M. M. Kessels, and M. C. M. van den Sanden, *N. J. Phys.* **9**, 280 (2007).
- ⁴²A. V. Shah, J. Meier, E. Vallat-Sauvain, N. Wyrsh, U. Kroll, C. Droz, and U. Graf, *Sol. Energy Mater. Sol. Cells* **78**, 469 (2003).
- ⁴³A. Gordijn, A. Pollet-Villard, and F. Finger, *Appl. Phys. Lett.* **98**, 211501 (2011).
- ⁴⁴A. J. Flikweert, J. Woerdenweber, B. Grootoonk, T. Zimmermann, and A. Gordijn, in *IEEE Proceedings of In-situ determination of silane gas utilization and deposition rate for different deposition regimes of $\mu\text{-Si:H}$ using FTIR and OES in-situ*, 2012, p. 1609.
- ⁴⁵B. Strahm, A. A. Howling, L. Sansonnens, and C. Hollenstein, *J. Vac. Sci. Technol. A* **25**, 1198 (2007).
- ⁴⁶H. Fujiwara, M. Kondo, and A. Matsuda, *Surf. Sci.* **497**, 333 (2002).
- ⁴⁷K. Nakamura, K. Yoshino, S. Takeoka, and I. Shimizu, *Jpn. J. Appl. Phys., Part 1* **34**, 442 (1995).
- ⁴⁸P. Roca i Cabarrocas, *J. Non-Cryst. Solids* **266–269**, Part 1, 31 (2000).
- ⁴⁹D. Han, G. Yue, J. D. Lorentzen, J. Lin, H. Habuchi, and Q. Wang, *J. Appl. Phys.* **87**, 1882 (2000).
- ⁵⁰J. I. Pankove, D. E. Carlson, J. E. Berkeyheiser, and R. O. Wance, *Phys. Rev. Lett.* **51**, 2224 (1983).
- ⁵¹Y. Sobajima, S. Kamanaru, H. Muto, J. Chantana, C. Sada, A. Matsuda, and H. Okamoto, *J. Non-Cryst. Solids* **358**, 1966 (2012).
- ⁵²Y.-M. Li, L. Li, J. A. A. Selvan, A. E. Delahoy, and R. A. Levy, *Thin Solid Films* **483**, 84 (2005).
- ⁵³S. N. Agbo, J. Krč, R. A. C. M. M. van Swaaij, and M. Zeman, *Sol. Energy Mater. Sol. Cells* **94**, 1864 (2010).
- ⁵⁴J. Müller, B. Rech, J. Springer, and M. Vanecek, *Sol. Energy* **77**, 917 (2004).